crystals

MDPI

Article

Efficient Dye Contaminant Elimination and Simultaneous Electricity Production via a Carbon Quantum Dots/TiO_2 Photocatalytic Fuel Cell

Zixuan Feng, Xuechen Li, Yueying Lv and Jie He *

School of Integrated Circuit Science and Engineering, Advanced Materials and Printed Electronics Center, Tianjin Key Laboratory of Film Electronic & Communication Devices, Tianjin University of Technology, Tianjin 300384, China; fzx2978997058@stud.tjut.edu.cn (Z.F.); lixuechen@stud.tjut.edu.cn (X.L.); lyy@stud.tjut.edu.cn (Y.L.)

* Correspondence: hejie@email.tjut.edu.cn

Abstract: Conventional wastewater treatment methods do not fully utilize the energy in wastewater. This study uses a photocatalytic fuel cell (PFC) to remove dye impurities and generate electricity with that energy. Pt serves as the PFC's cathode, while the carbon quantum dots (CQDs)/anatase TiO_2 (A-TiO_2) serve as its photoanode. The visible light absorption range of A-TiO_2 can be increased by combining CQDs with A-TiO_2. The composite of CQD and A-TiO_2 broadens the absorption edge from 364 nm to 538 nm. TiO_2's different crystal structures and particle sizes impact the PFC's power generation and dye contaminant removal. The 30 min photodegradation rate of methylene blue by the 20 nm A-TiO_2 was 97.3%, higher than that of the 5 nm A-TiO_2 (75%), 100 nm A-TiO_2 (92.1%), and A-TiO_2 (93%). The photocurrent density of the 20 nm A-TiO_2 can reach 4.41 mA/cm^2, exceeding that of R-TiO_2 (0.64 mA/cm^2), 5 nm A-TiO_2 (1.97 mA/cm^2), and 100 nm A-TiO_2 (3.58 mA/cm^2). The photodegradative and electrochemical test results show that the 20 nm A-TiO_2 delivers a better degradation and electrochemical performance than other samples. When the 20 nm A-TiO_2 was used in the PFC photoanode, the photocurrent density, open-circuit voltage, and maximum power density of the PFC were found to be 0.6 mA/cm^2, 0.41 V, and 0.1 mW/cm^2, respectively. The PFC prepared in this study shows a good level of performance compared to recent similar systems.

Keywords: CQDs; TiO_2; photocatalysts; photocatalytic fuel cell

Citation: Feng, Z.; Li, X.; Lv, Y.; He, J. Efficient Dye Contaminant Elimination and Simultaneous Electricity Production via a Carbon Quantum Dots/TiO_2 Photocatalytic Fuel Cell. *Crystals* **2024**, *14*, 1083. https://doi.org/10.3390/cryst14121083

Academic Editors: Sulakshana Shenoy and Chitiphon Chuaicham

Received: 14 November 2024
Revised: 12 December 2024
Accepted: 14 December 2024
Published: 16 December 2024

1. Introduction

With industrialization and increased energy use, the human society is becoming increasingly aware of the need to address environmental and energy issues [1]. Water pollution, as one of the various environmental problems, has received widespread attention [2]. Dye pollutants are among the many organic pollutants found in wastewater that are challenging to treat [3]. Research has demonstrated that a substantial amount of chemical energy is present in the organic pollutants found in wastewater [4]. Nevertheless, conventional techniques for treating wastewater, like precipitation by chemicals and physical absorption, are limited to the purification of wastewater; they are unable to fully harness its chemical energy [5]. Thus, one of the best approaches to address the energy crisis and water contamination is to transform chemical power into electrical power and remove the organic contaminants [6]. In recent years, photocatalysis (PC) technology has gained a lot of interest as an emerging field [7]. Its principle is based on the redox capacity of photocatalysts under light conditions, thus achieving the purpose of purifying pollutants [8]. Fuel cell (FC) technology and semiconductor PC technology have been combined into the photocatalytic fuel cell (PFC) technology [9]. This technology is capable of achieving two functions simultaneously: the generation of power and the effective breakdown of organic contaminants [10]. This technique shows promise in mitigating the energy crisis and reducing water pollution [11].

Transparent conductive oxide (TCO) films have been widely used in photovoltaic applications, such as solar cells, owing to their excellent optical transparency (more than 80%) and high electrical conductivity (~10^3 Ω^{-1} cm^{-1} or higher) in the visible spectral range [12]. TCOs are degenerated wide-bandgap semiconductors such as In_2O_3 highly doped by Sn (ITO), ZnO highly doped by Al (AZO), ZnO highly doped by doped B (BZO), and SnO_2 highly doped by F (FTO) [13]. The main component of FTO is SnO_2, and, compared with In in ITO, Sn is a more common and less expensive metal [14]. Therefore, in this work, FTO was used as an alternative to ITO. TiO_2 is characterized by a low cost, the availability of different inexpensive precursors, chemical stability, and non-toxicity [15], and TiO_2 can be excited by light to produce e^- with strong reducing properties and h^+ with strong oxidizing properties, making TiO_2 an efficient photocatalyst [16]. However, TiO_2 has a large forbidden band width, typically between 3.0 eV and 3.2 eV [17]. This makes it absorb, mainly, UV light and weakly absorb visible light. In order to solve this problem, Lu et al. investigated the effect of doping Rh, Pb, Pt, Au, and other noble metals on the properties of TiO_2, and the results show that the doping of noble metals significantly red-shifted the spectral absorption range of the material, a phenomenon which enhanced the photoresponsiveness of the material in the visible light. Through formaldehyde photocatalytic oxidation-related experiments, the results show that the degradation efficiency of TiO_2 with respect to formaldehyde can be enhanced more obviously by using the precious metal doping method [18,19]. Studies have shown that a TiO_2 coating can be used as an interfacial adjustment layer between the transparent conductive layer and the electrochromic layer in electrochromic smart windows [20]. The high conductivity of TiO_2 coatings plays a key role when they are used as working electrodes in electrochromic devices. During the electrochromic process, the TiO_2 coating is able to conduct electrons efficiently so that the electrochromic reaction can proceed smoothly [21,22]. TiO_2 coatings are also used as single and multilayer anti-reflective coatings for solar cells [23,24]. Huang et al. successfully prepared TiO_2/ZnO double-layer coatings with broadband reflectance reduction and downshift capabilities, and the average reflectance of the coated samples in the 400–1100 nm band was 5.29%, which was 24.97% lower than that of the uncoated samples [25]. With its high surface area, excellent optoelectronic properties, and chemical stability, TiO_2 nanoparticles have become important materials for a wide range of sensors for gases, humidity, biology, electrochemistry, and temperature [26]. Carbon quantum dots (CQDs) are monodispersed graphite particles with a diameter smaller than 10 nm that have unique properties such as light-harvesting, photo-induced electron transfer, electron reservoir, and tunable photoluminescence [27]. The incorporation of CQDs into TiO_2, with C substituting some of the lattice O atoms, enables the TiO_2 composite photocatalyst to effectively absorb light at wavelengths below 535 nm [28]. Catalytic efficiency can be significantly increased by using composites of TiO_2 and CQDs which can facilitate the interfacial electron transition and separation of photogenerated carriers [29,30]. Jung et al. investigated the properties of carbon-doped TiO_2 and found that it could produce enhanced photocatalytic reactions in the visible light [31].

In this paper, CQDs/TiO_2 composites are used as photoanodes for a PFC. Firstly, the TiO_2 with optimal photocatalytic and electrochemical performances was selected through experiments. Although TiO_2 has a good photocatalytic ability, it cannot absorb the visible light. TiO_2 can be modified with CQDs to increase its capacity to absorb light and decrease its band gap (E_g), an approach which enhances its photocatalytic performance. The absorption edges of the CQDs/TiO_2 composites extend into the visible region, providing more active sites for the PFC reaction. This PFC can generate electricity while removing dye contaminants (RhB).

2. Materials and Methods

2.1. Materials

Sodium sulfate (Na_2SO_4, 99+%), anhydrous ethanol (C_2H_6O, 99.5+%), rhodamine B (RhB, 99.8+%), disodium ethylenediaminetetraacetate (EDTA-2Na, 99+%), rutile TiO_2

(R-TiO_2, 99+%), and 5 nm, 20 nm, and 100 nm anatase TiO_2 (A-TiO_2, 99+%) were supplied by Tianjin Damao Chemical Reagent Factory (Tianjin, China). Jining Liduo Chemical Co. (Jining, China) provided methylene blue (MB, 99.8+%). Thermo Fisher Scientific (Shanghai, China) provided the citric acid (CA, 99+%). Beijing Chemical Reagent Company (Beijing, China) supplied the urea. Tianjin Kewei Chemical Co., Ltd. (Tianjin, China) supplied the isopropanol (IPA, 99+%) and benzoquinone (BQ, 99+%).

2.2. Material Preparation

2.2.1. Preparation of CQDs

A total of 1 L of deionized water had 100 g of CA and 100 g of urea dissolved in it. After that, the resultant solution was exposed to 700 W microwave radiation for 5 min. To re-suspend the precipitate in the water, 1 L of deionized water was added after the 5 min period. After that, the synthesized CQDs were centrifuged for 20 min at 6000 rpm in reusable centrifuge tubes to remove any suspended contaminants [32].

2.2.2. Preparation of CQDs/A-TiO_2

A total of 50 mg, 70 mg, and 100 mg of A-TiO_2 was mixed with 5 mL of CQD solution, respectively. Then, the mixed solutions were magnetically stirred for 2 h to ensure that A-TiO_2 could be uniformly mixed in the CQD solution. In order to produce the composite photocatalysts with 5%, 7%, and 10% CQDs/A-TiO_2, the final solutions were subjected to a 12 h drying process at 80 °C in a vacuum oven. The percentages of 5%, 7%, and 10% refer to the CQD content of A-TiO_2.

2.2.3. Preparation of FTO/CQDs/A-TiO_2 Photoanode

The FTO (2 cm × 1 cm) was used as the substrate. It was cleaned with anhydrous ethanol and deionized water. A total of 10 mg of CQDs/A-TiO_2 was mixed with 1 mL of anhydrous ethanol, 1 mL of deionized water, and 20 µL of Nafion by ultrasonication. The combined solution was drop-casted onto the FTO and left to cure at room temperature for 12 h in order to generate the photoanode.

2.3. Characterization

An X-ray diffractometer (XRD, Rigaku Ultima IV, Rigaku Corporation, Tokyo, Japan) was used to study the crystal structures of the materials. X-ray photoelectron spectroscopy (XPS, ESCALAB250Xi, ThermoFisher-VG Scientific, Waltham, MA, USA) was used to determine the composition and valence states. The morphologies of the photoanodes were characterized using a scanning electron microscope (SEM; Verios 460L, FEI, Hillsboro, OR, USA) and a high-resolution transmission electron microscope (HRTEM; Talos F200 X, FEI, Hillsboro, OR, USA). The ultraviolet visible spectrophotometer (UV-VIS) absorption spectra of the materials were analyzed using a UV-VIS DRS (UV-VIS DRS, Lambda 750 UV/VIS/NIR, PerkinElmer, Shelton, CT, USA). Fourier transform infrared (FTIR) spectroscopy of the 10% CQDs/A-TiO_2 was performed using an FTIR spectrometer (Shimadzu 4100, Thermo Nicolet, Thermo Fisher Scientific, Waltham, MA, USA) with a spectral range of 4000~450 cm^{-1} and a resolution of 32 cm^{-1} at room temperature.

2.4. Measurement of Photodegradation

A total of 10 mg of sample (5 nm, 20 nm, 100 nm A-TiO_2 or R-TiO_2) was mixed with 25 mL of MB (10 mg/L) solution to measure the photodegradation performance of the sample. Before the photodegradation was initiated, the solution was magnetically stirred for 20 min to achieve the adsorption equilibrium. Then, the photodegradation experiment was conducted under 90 mW/cm^2 UV irradiation. A sample of 3.5 mL of the solution at the 10 min, 20 min, 30 min, 50 min, 70 min, and 90 min intervals was centrifuged for 10 min at 10,000 rpm during the photodegradation process. After centrifugation, the resultant supernatants were put in cuvettes and a UV-VIS spectrophotometer was used to detect

the UV absorption spectra of MB. The following equation was used to determine the photodegradation performance:

$$D = (C_0 - C_t)/C_0 \times 100\% = (A_0 - A_t)/A_0 \quad (1)$$

In this case, A_0 represents the initial intensity of the RhB absorption peak at 662 nm, A_t denotes the intensity of the RhB absorption peak at time t, C_0 represents the initial concentration of RhB, and C_t represents the concentration of the RhB solution degraded at the moment t.

Stability testing: after each photocatalytic reaction, the samples were centrifuged, ultrasonically cleaned, and dried for reuse.

2.5. Photoelectrochemical (PEC) Measurements of Electrodes

PEC tests were carried out using a three-electrode setup on an electrochemical workstation (Versa STAT 3, Princeton, Oak Ridge, TN, USA), which was lit by a 300 W xenon lamp that produced a 30 mW/cm^2 UV source. The electrolyte for the PEC test was an aqueous solution of Na_2SO_4 at 0.5 mol/L. A Pt wire served as the counter electrode (CE), Ag/AgCl (3.5 mol/L KCl) served as the reference electrode (RE), and the working electrode (WE) was a 5% (7%, 10%) CQDs/A-TiO_2 film electrode. The turn-on voltage of the photoanode 10% CQDs/A-TiO_2 and the turn-on voltage of the cathode Pt were tested through an electrochemical workstation in the range of −1 V to 1 V against a reversible hydrogen electrode (RHE). Transient current response tests were performed with a constant voltage of 0 V for comparison with RHE under interval illumination.

2.6. PFC Measurements

A 300 W xenon lamp delivered 30 mW/cm^2 UV source irradiation for the PFC measurements, which were conducted using an electrochemical workstation (Versa STAT 3, Princeton, Oak Ridge, TN, USA) with a two-electrode setup. A 10% CQDs/A-TiO_2 film electrode served as the photoanode, Pt wire served as the cathode, and 0.5 mol/L RhB aqueous solution served as the fuel. The photocurrent density, open-circuit voltage, and polarization curves of the PFC were tested and collected using an electrochemical workstation. Finally, the ability of the PFC to degrade RhB was tested at 0 V and 0.2 V bias to simulate the ability of the PFC to degrade dye contaminants.

3. Results

3.1. Composition, Structure and Morphology

The XRD analysis was conducted to investigate the crystal structures of A-TiO_2 and 10% CQDs/A-TiO_2, as shown in Figure 1. As it can be seen in Figure 1, the diffraction peaks were located at 2θ = 27.4°, 36.6°, 39.6°, 42.3°, 44.1°, 54.7°, 56.8°, 63.5°, 65.3°, 69.8°, and 70.2°, corresponding to the (110), (101), (200), (111), (210), (211), (220), (002), (310), (221), and (301) crystal planes of R-TiO_2, respectively (JCPDS, 73–2224) [33]. The peaks at 2θ = 25.3°, 36.9°, 37.7°, 38.6°, 48°, 53.8°, 55°, 62.8°, 68.9°, 70.3°, 75.1°, 76°, and 82.7° can be assigned to the (103), (004), (112), (200), (105), (211), (204), (116), (202), (301), (215), and (224) planes of the A-TiO_2 (CPDS 2–387), respectively [34]. Upon the synthesis of 10% CQDs/A-TiO_2, it was noted that there were no substantial alterations in the peaks. This phenomenon can be accounted for by the relatively low concentration of CQDs within the 10% CQDs/A-TiO_2 composite. As a result, their peaks were found to be efficiently superimposed upon those of A-TiO_2 [35].

SEM was used to examine the surface morphology of the catalysts. Figure 2a,b shows the SEM morphology of A-TiO_2 and 10% CQDs/A-TiO_2. It is evident that the A-TiO_2 particle size ranged from 20 nm to 30 nm, and, since the CQDs' diameter was only a few nanometers, it had little bearing on the 10% CQDs/A-TiO_2 morphology. The SEM images of the 10% CQDs/A-TiO_2 mainly show the A-TiO_2 structure [36]. In order to further confirm the composition of the 10% CQDs/A-TiO_2, EDS tests were performed. Figure S2 shows that the EDS test results indicate that the elements C, O, and Ti were uniformly distributed in

the material, further confirming the successful combination of CQDs and TiO_2. It is evident from the TEM images presented in Figure 2c,d that the lattice spacing measured 0.35 nm, corresponding to the (101) crystal plane of A-TiO_2. This, therefore, serves as an indication of the presence of A-TiO_2 [30]. Figure 2d clearly shows the uniform distribution of CQDs, with a particle size of about 3 nm, on A-TiO_2. These results demonstrate the successful preparation of A-TiO_2 and 10% CQDs/A-TiO_2. As it can be seen from Figure S1, R-TiO_2 exhibited elongated particles closely fitting together. R-TiO_2 had a grain size of 140 nm in the length direction and of 60 nm in the width direction.

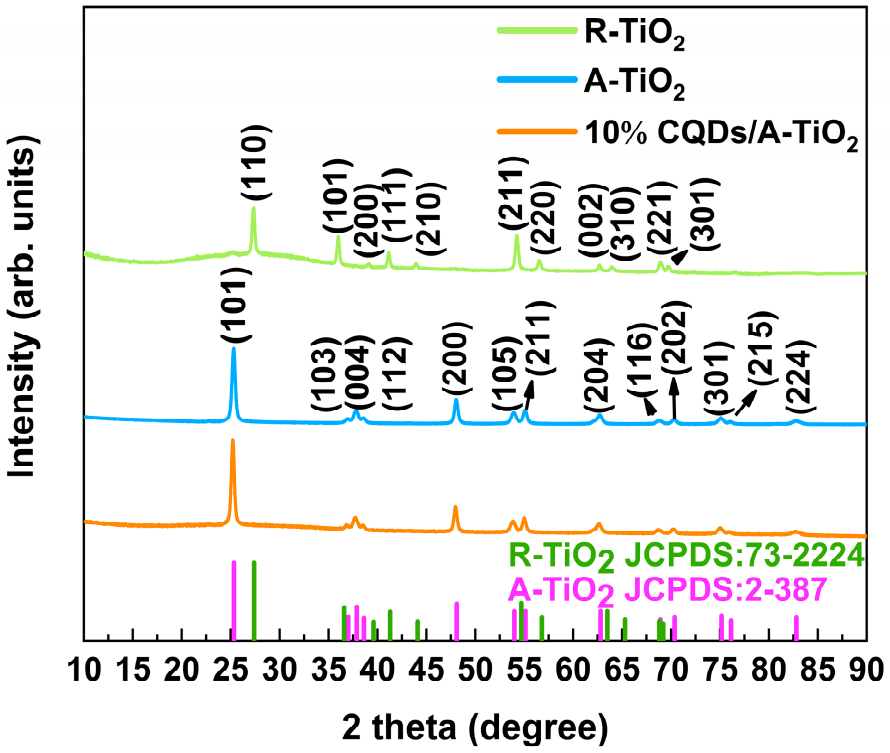

Figure 1. XRD of R-TiO_2, A-TiO_2, and 10% CQDs/A-TiO_2.

A-TiO_2 and 10% CQDs/A-TiO_2 were tested using XPS. The full XPS spectra of A-TiO_2 and 10% CQDs/A-TiO_2, shown in Figure 3a, indicate that the prepared photoanodes contained mainly Ti, O, and C elements [37]. The O 1s spectra of A-TiO_2 had two primary peaks at 529.8 eV and 531.4 eV, respectively, corresponding to Ti-O and Ti-OH, as seen in Figure 3b [38]. By observing the O 1s spectra of the 10% CQDs/A-TiO_2, it is clear that the main peaks occurred at 530 eV and 531.6 eV. The 10% CQDs/A-TiO_2 main peak binding energies all experienced an increase of 0.2 eV. The spectra of C 1s of A-TiO_2 in Figure 3c show that C-C, C-O, and O-C-Ti are represented by the three peaks at 284.7 eV, 286.2 eV, and 288.7 eV, respectively [34]. The primary peak's binding energy was found to remain unchanged based on the 10% CQDs/A-TiO_2 C 1s spectra. The peaks at 458.6 eV (Ti $2p_{3/2}$) and 464.3 eV (Ti $2p_{1/2}$) in the Ti 2p of the A-TiO_2 spectrum in Figure 3d show that Ti existed mainly in the form of Ti^{4+} [39]. The Ti 2p spectra of 10% CQDs/A-TiO_2 demonstrate that, upon combination of CQDs and A-TiO_2, the binding energies of both Ti $2p_{3/2}$ and Ti $2p_{1/2}$ exhibited a slight increment. By continuing to examine the 2p spectrum of 10% CQDs/A-TiO_2 in Figure 3d, it can be observed that the peak at 457.6 eV showed a small peak due to the formation of a small amount of Ti^{3+} [40].

UV-VIS was used to evaluate the optical characteristics of R-TiO_2, A-TiO_2, and 10% CQDs/A-TiO_2. Reasonably speaking, Figure 4a shows that the prepared A-TiO_2's absorption edge lied at 364 nm, and that it was only responsive to UV light [41]. By observing Figure 4a, it can be seen that the absorption edge of the prepared R-TiO_2 was located at 338 nm. After the combination of CQDs and A-TiO_2, the absorption edge increased to

538 nm. This is because the C-O-Ti bonding between A-TiO_2 and CQDs lowers the band edge's absorption energy and extends it into the visible part of the spectrum [42]. Thus, the system's overall light absorption capability was enhanced by the combination of CQDs and A-TiO_2. The E_g of A-TiO_2 and 10% CQDs/A-TiO_2 can be estimated from the Tauc plot, which can be determined using the following formula:

$$(\alpha h)^2 = A(h\upsilon - E_g) \quad (2)$$

$$h\upsilon = h\frac{c}{\lambda} \quad (3)$$

where λ is the wavelength, υ is the illumination frequency, α is the absorption coefficient, A is the constant, c (3×10^8 m·s $^{-1}$) is the speed of light, and h (6.626×10^{-34} J·Hz^{-1}) is the Planck constant. By observing Figure 4b, it can be seen that the E_g of R-TiO_2 was 3.7 eV. The E_g of 10% CQDs/A-TiO_2 decreased to 2.8 eV, as seen in Figure 4b, indicating that the photoanode's E_g may be lowered by a combination with CQDs.

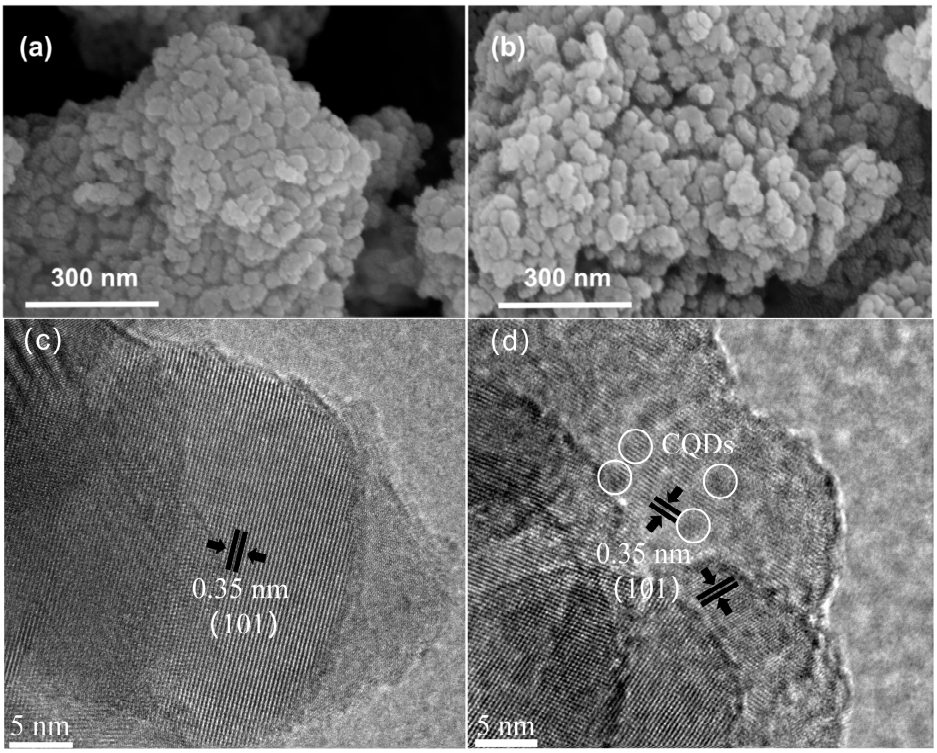

Figure 2. SEM images of (**a**) A-TiO_2 and (**b**) 10% CQDs/A-TiO_2; TEM images of (**c**) TiO_2 and (**d**) 10% CQDs/A-TiO_2.

The presence of different functional groups on the surface of the 10% CQDs/A-TiO_2 sample was confirmed by FTIR spectroscopy, as shown in Figure 5. The 3286 cm^{-1} band was attributed to the -OH group on the surface of TiO_2 which is believed to be crucial in the photocatalytic process. This is because it traps light-generated electrons and holes to produce reactive oxygen species [43]. The band in the 2981 cm^{-1} range was attributed to the O-H stretching of the adsorbed water molecules. The absorption bands at 1700 cm^{-1} and 1514 cm^{-1} were stretched to stretching vibrations of C=C and C-O groups, respectively, indicating the presence of elemental C on the catalyst's surface [44]. The appearance of absorption at 568 cm^{-1} in Figure 5 confirms the synergistic effect of Ti-O-Ti and Ti-O-C vibrations, as reported by Zhang et al. [45].

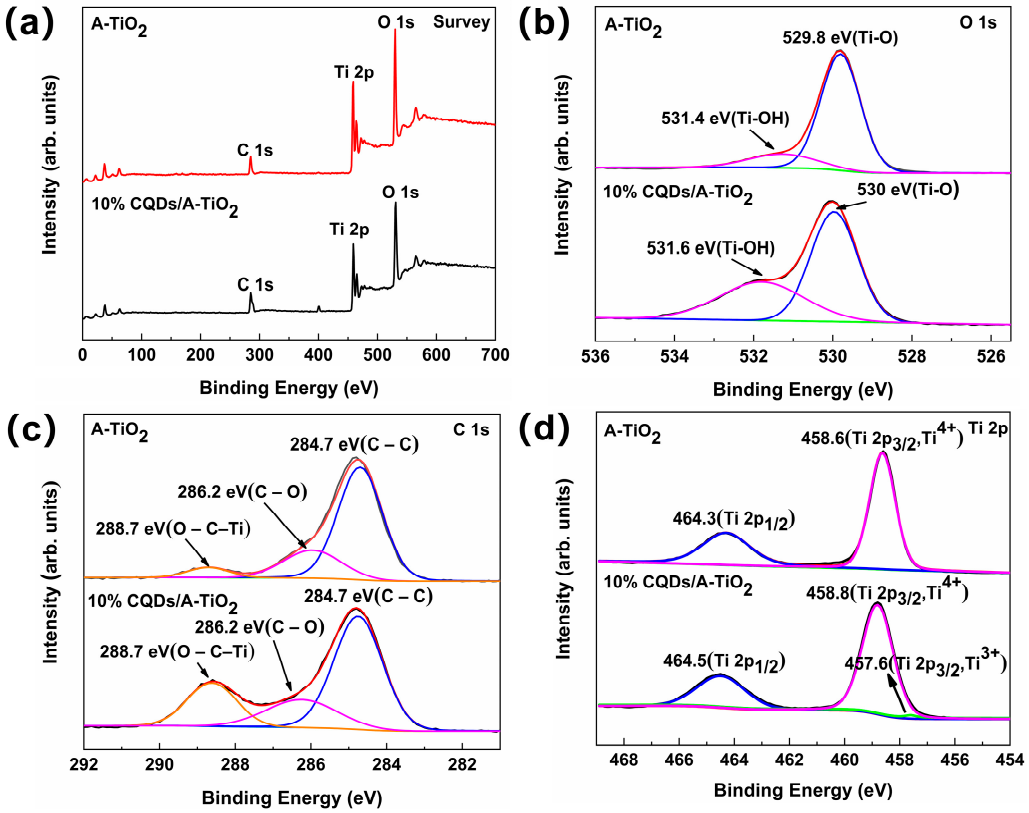

Figure 3. The A-TiO_2 and 10% CQDs/A-TiO_2 XPS spectra: (**a**) survey spectra, (**b**) O 1s, (**c**) C 1s, and (**d**) Ti 2p.

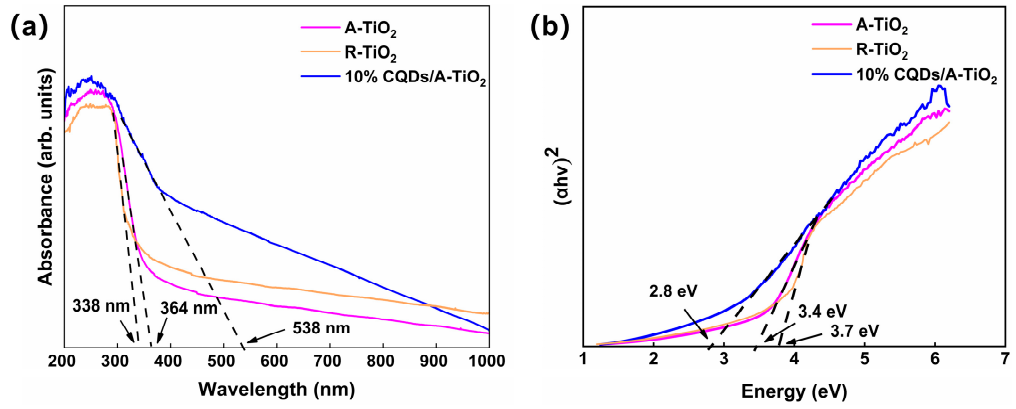

Figure 4. (**a**) Typical UV-VIS absorption spectra and (**b**) the Tauc plot of R-TiO_2, A-TiO_2, and 10% CQDs/A-TiO_2.

3.2. Photocatalytic Properties of the Photoanode

MB is an organic pollutant that can cause significant mortality among aquatic animals at high concentrations [46]. In order to verify the effectiveness of different crystal types and particle sizes of TiO_2 at treating environmental pollution, the degradation properties of A-TiO_2 at 5 nm, 20 nm, and 100 nm, as well as R-TiO_2, were tested in relation to the degradation of the MB solution under UV light. Figure S3a–d shows that all four photocatalysts were able to completely disintegrate the MB solution within 90 min. As illustrated in Figure 6a, the rate of photodegradation of MB by the 20 nm A-TiO_2 was 97.3% in 30 min, surpassing the rates of the 5 nm A-TiO_2 (75%), 100 nm A-TiO_2 (92.1%), and R-TiO_2 (93%). The photocatalytic performance was significantly influenced by the specific surface area of the TiO_2 particles. The specific surface area of the TiO_2 particles increases with a

decreasing particle size. A greater surface area allows for a greater area of contact between the organic pollutants and the photocatalyst, increasing the photocatalytic activity [47]. However, compared to the 20 nm A-TiO_2, the degradation rate of the 5 nm A-TiO_2 was lower, indicating that A-TiO_2's specific surface area was not the only factor influencing its photocatalytic efficacy. The recombination of holes and electrons is supported by an increase in the density of recombination centers which occurs when the particle size decreases [48]. Consequently, the 5 nm A-TiO_2's photocatalytic performance was diminished. Compared to R-TiO_2, A-TiO_2 had a better photocatalytic performance. This is because the crystal structure of A-TiO_2 exhibits tetrahedral coordination with a higher surface activity, while the crystal structure of R-TiO_2 exhibits hexahedral coordination with a lower surface activity and is more stable [49]. Since the degradation performance of the 20 nm A-TiO_2 was optimal, the 20 nm A-TiO_2 was subsequently combined with CQDs to form a 10% CQDs/A-TiO_2 composite photocatalyst. As shown in Figure 6a, the photodegradation rate of MB by the 10% CQDs/A-TiO_2 was 91.3% after 10 min, and MB was completely degraded after 30 min.

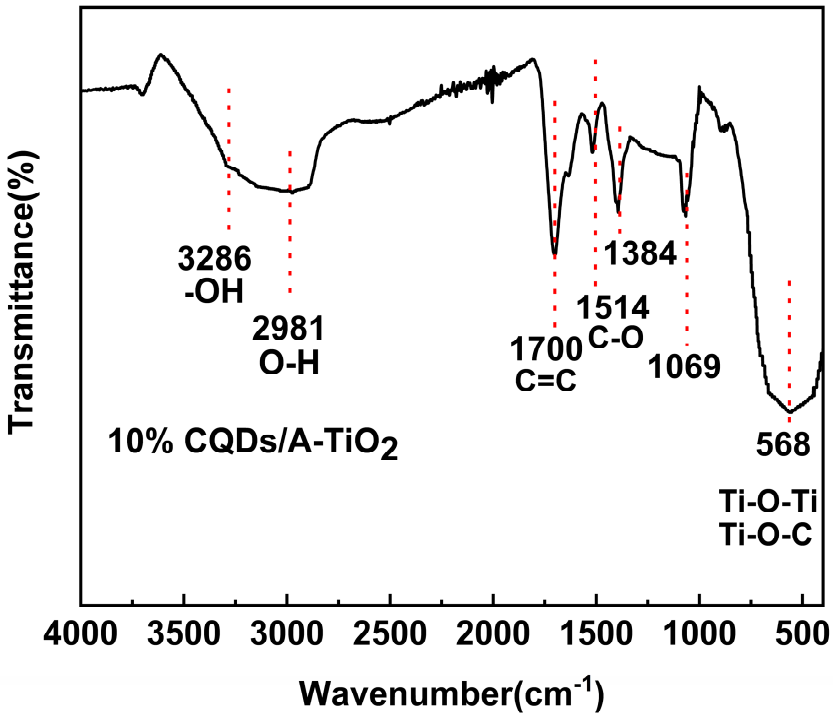

Figure 5. FTIR spectra of 10% CQDs/A-TiO_2.

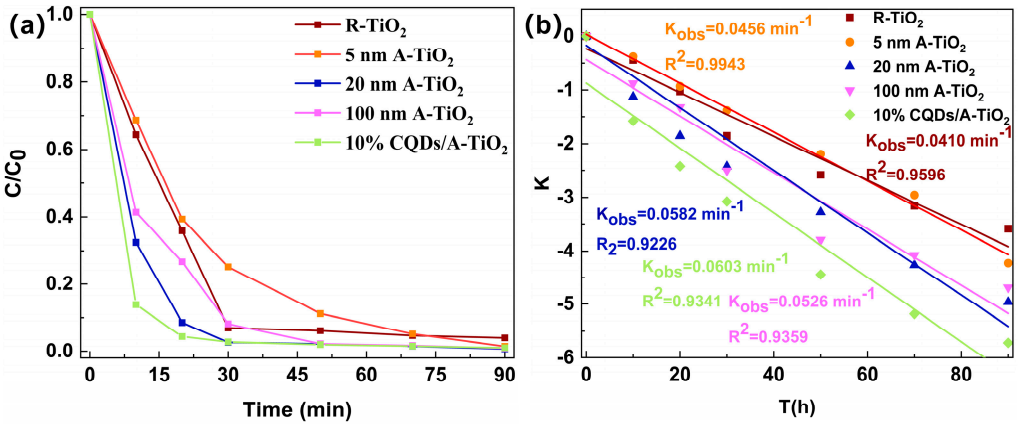

Figure 6. Photodegradation curves (**a**) and pseudo-first-order rate kinetics curves of (**b**) R-TiO_2, 5 nm A-TiO_2, 20 nm A-TiO_2, 100 nm A-TiO_2, and 10% CQDs/A-TiO_2.

Figure 6b shows the photodegradation curves of the quasi-primary kinetic model for each sample. From Figure 6b, it can be seen that the kinetic constants of R-TiO_2, 5 nm A-TiO_2, 20 nm A-TiO_2, 100 nm A-TiO_2, and 10% CQDs/A-TiO_2 were 0.0410 min^{-1}, 0.0456 min^{-1}, 0.05820 min^{-1}, 0.0526 min^{-1}, and 0.0603 min^{-1}, respectively. The results show that the 20 nm A-TiO_2 delivered the best degradation performance. The degradation performance was further enhanced by the addition of CQDs to A-TiO_2. Figure S4 shows that the degradation rate of each sample was 99.05% after 20 min of adsorption. After 30 min, the degradation rate was 98.98%. In order to evaluate the photochemical stability of the catalysts, replicate experiments of MB photodegradation were performed on the 10% CQDs/A-TiO_2 samples. Figure S5 shows that 97% of MB was degraded after 30 min when using the 10% CQDs/A-TiO_2 sample. After five cycles, the photocatalytic activity of the 10% CQDs/A-TiO_2 decreased, and 91% of MB was degraded after 30 min. The photocatalytic activity of 10% CQDs/A-TiO_2 decreased by 6% after repeated use over five cycles, indicating that the photocatalyst has excellent photochemical stability.

In order to further investigate the photocatalytic mechanism and find out which free radicals dominate during the photocatalytic degradation of MB, free radical trapping experiments were then performed on 10% CQDs/A-TiO_2. In this work, IPA, EDTA-2Na, and BQ were used as sacrificial agents for hydroxyl radicals (•OH), cavities, and superoxide radicals ($\bullet O^{2-}$), respectively. As shown in Figure S6, the photocatalytic rate decreased by 13% when IPA was used as an •OH sacrificial agent, indicating that •OH plays a weak role in the degradation process. The photocatalytic rate was reduced by 50% when EDTA-2Na was used as a hole scavenger. When BQ was added as an $\bullet O^{2-}$ sacrificial agent, the degradation rate decreased most significantly with the extension of the illumination time, and its photocatalytic rate decreased by 80%. This result indicates that $\bullet O^{2-}$ dominates the photodegradation process.

3.3. The Performance of PEC

PEC tests of 5 nm, 20 nm, 100 nm A-TiO_2, and R-TiO_2 were performed using a three-electrode structure. According to Figure 7a, the photocurrent density of 20 nm A-TiO_2 may reach 4.41 mA/cm^2, which is greater than that of R-TiO_2 (0.64 mA/cm^2), 5 nm A-TiO_2 (1.97 mA/cm^2), and 100 nm A-TiO_2 (3.58 mA/cm^2). Therefore, combined with the previous experimental results from the photodegradation experiments, the following experiments were performed with the 20 nm A-TiO_2 samples.

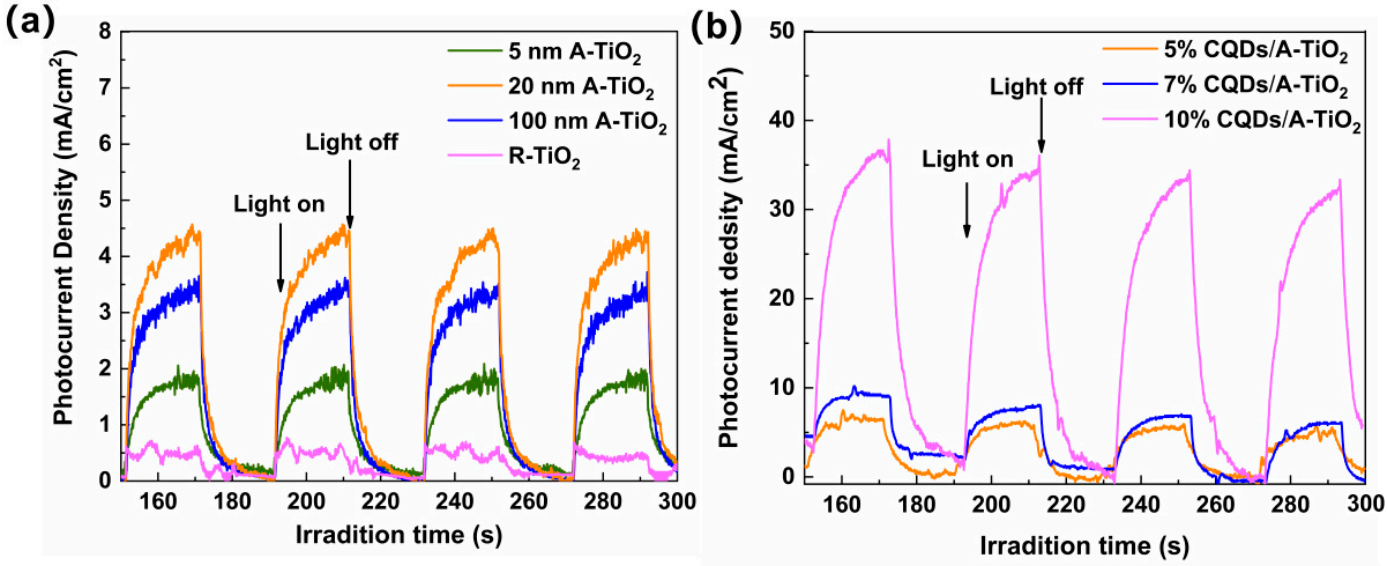

Figure 7. Photocurrent density profiles of (**a**) A-TiO_2 with different particle sizes and R-TiO_2 and (**b**) different ratios of CQDs/A-TiO_2.

Three-electrode structures were used to study the photocurrent density of catalysts containing 5%, 7%, and 10% of CQDs/A-TiO_2. In Figure 7b, we can observe that the photocurrent density of 10% CQDs/A-TiO_2 was 34.63 mA/cm^2, a significantly higher value than that of 5% CQDs/A-TiO_2 (5.62 mA/cm^2) and 7% CQDs/A-TiO_2 (6.74 mA/cm^2). The above results show that the 10% CQDs/A-TiO_2 structure has the best PEC performance. The 10% CQDs/A-TiO_2 was found to be the ideal addition ratio, and it was discovered that the electrochemical performance increased with the addition of CQDs. Modest CQD compounding can enhance TiO_2's photocatalytic performance for two reasons. Firstly, it is ascribed to the doping of CQDs, during which C replaces the lattice O atoms in TiO_2. More active sites for the PEC reaction are created when C-O-Ti bonds are formed between CQDs and TiO_2, resulting in a drop in band-edge absorption energy and an extension of TiO_2's absorption edge into the visible region [50]. Secondly, by inhibiting the recombination of photogenerated carriers, CQDs can facilitate the transport of electrons from the conduction band of A-TiO_2 to the organic contaminants [51]. The turn-on voltage was tested for the 10% CQDs/A-TiO_2 photoanode and the Pt cathode. The photoanode's turn-on voltage was 0.16 V, whereas the Pt cathode's turn-on voltage was 0.64 V, as seen in Figure S7.

3.4. The Performance of PFC

Using Pt as the cathode, RhB as the fuel, and the fabricated 10% CQDs/A-TiO_2 thin film electrode as the photoanode, the PFC was assembled. By testing the electrochemical properties of the PFC, the corresponding photocurrent density, discharge curve, and power density were obtained. It is evident from Figure 8a,b that the PFC's open-circuit voltage was 0.41 V and its short-circuit current density was 0.6 mA/cm^2. In Figure 8c,d, the power density curves and the polarization curves of the PFC are displayed. The vertical intercepts of the polarization curves correspond to the open-circuit voltage, while the horizontal intercept corresponds to the short-circuit current density. The PFC had a maximum power density of 0.1 mW/cm^2 and a photocurrent density of 0.6 mA/cm^2, respectively. The photodegradation curves of RhB by the PFC at 0.2 V and 0 V voltage are displayed in Figure 9. It is evident that, when the voltage was increased, the PFC's capacity to eliminate dye contaminants also increased. The schematic diagram of the PFC during dye degradation is shown in Figure S8.

To further evaluate the value of the 10% CQDs/A-TiO_2 proposed in this study, we compared its performance with that of similar PFC systems reported recently in the literature. The photocurrent density, open-circuit voltage, and maximum power density of the PFC from the present work were found to be higher than most reports (Table S1). The results indicate that the PFC constructed using the 10% CQDs/A-TiO_2 in this study delivers an excellent performance.

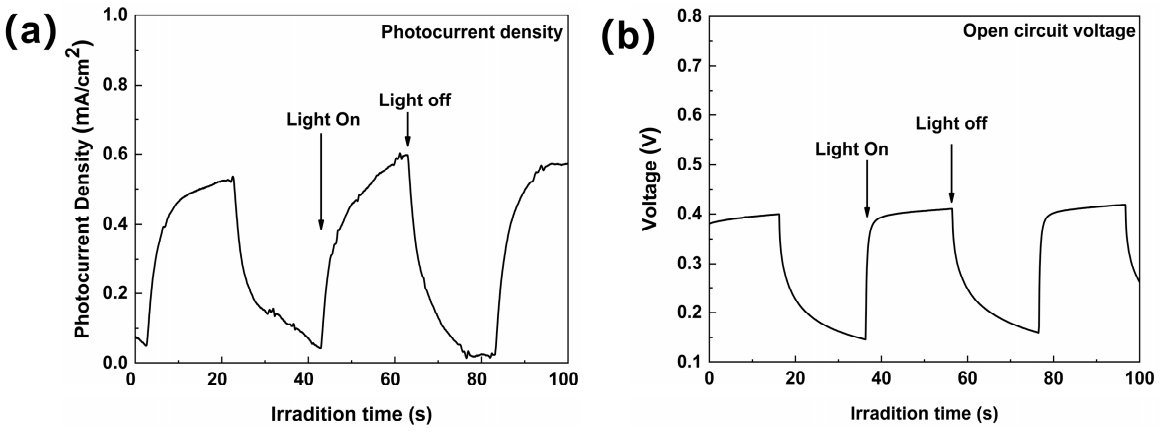

Figure 8. *Cont.*

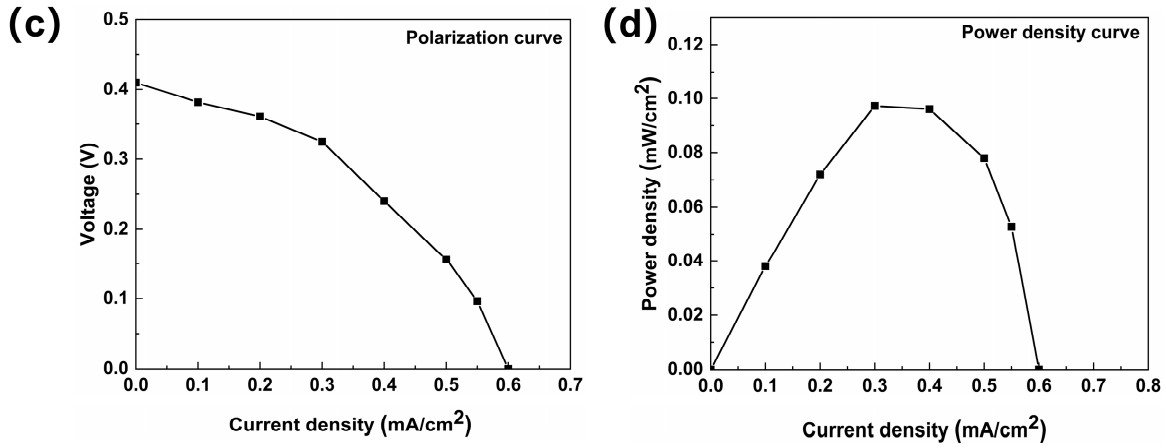

Figure 8. PFC: (**a**) photocurrent density curve; (**b**) open-circuit voltage curve; (**c**) polarization curve; (**d**) power density curve.

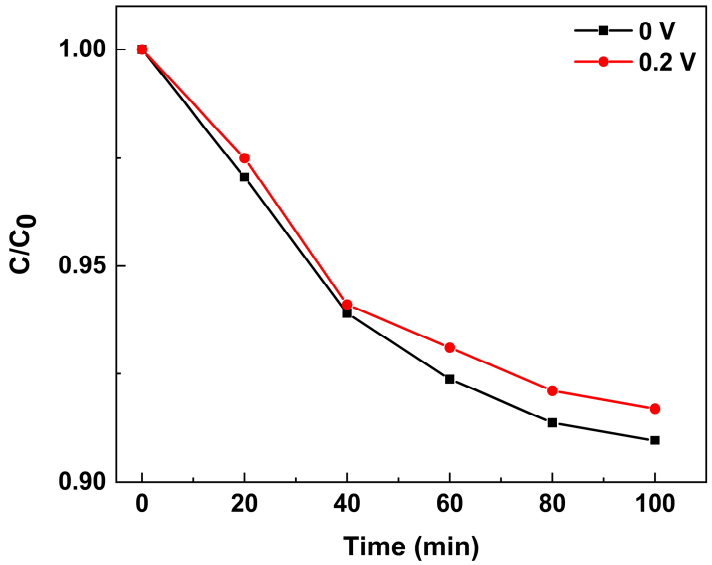

Figure 9. Photodegradation curves of PFC at different voltages.

4. Conclusions

In this study, a PFC is prepared to remove dye contaminants and generate electricity at the same time. Composites of CQDs and TiO_2 are chosen to serve as the PFC's photoanode. Visible light absorption is enhanced by the composite CQDs/TiO_2 photoanodes. The PFC produces an open-circuit voltage of up to 0.41 V and a photocurrent density of 0.6 mA/cm^2. The maximum power density of the PFC is 0.1 mW/cm^2. The photocatalytic activity and electrochemical performance of the 5 nm, 20 nm, 100 nm A-TiO_2, and R-TiO_2 are investigated for the photocatalytic degradation of organic dyes under UV light. The 20 nm A-TiO_2 demonstrates the best photocatalytic efficiency and electrochemical performance compared to the 5 nm and 100 nm A-TiO_2 and R-TiO_2. Under UV light, the electrochemical characteristics of the 5%, 7%, and 10% CQDs/A-TiO_2 are examined. The results show that the 10% CQDs/A-TiO_2 delivers the best electrochemical performance.

Supplementary Materials: The following supporting information can be downloaded at: https://www.mdpi.com/article/10.3390/cryst14121083/s1, Figure S1: SEM images of R-TiO_2; Figure S2: (a) SEM of 10% CQDs/A-TiO_2, (b) C, (c) O, and (d) Ti are EDS elemental maps of 10% CQDs/A-TiO_2; Figure S3: The UV-VIS absorption spectra of (a) R-TiO_2 and A-TiO_2 at (b) 5 nm, (c) 20 nm, and (d) 100 nm; Figure S4: Adsorption test of R-TiO_2, 5 nm A-TiO_2, 20 nm A-TiO_2, 100 nm A-TiO_2, and 10% CQDs/A-TiO_2; Figure S5: Stability of 10% CQDs/A-TiO_2 under UV irradiation; Figure S6:

Photocatalytic degradation curves with different sacrificial agents added to the 10% CQDs/A-TiO_2; Figure S7: The turn-on voltage of (a) 10% A-TiO_2/CQDs and (b) Pt. Figure S8: Schematic diagram of a PFC cell during dye degradation; Table S1: Comparison of the performance of PFC with other operations. References [52–55] are included in the Supplementary Material.

Author Contributions: Conceptualization, Z.F. and J.H.; methodology, Z.F.; writing—original draft preparation, Z.F.; formal analysis, Z.F. and J.H.; investigation, X.L.; software, Y.L.; writing—review and editing, J.H.; funding acquisition, J.H. All authors have read and agreed to the published version of the manuscript.

Funding: This research was funded by the Key Research and Development Program of Tianjin City (Grant No. 22YFYSHZ00280) and by the National Natural Science Foundation of China (Grant No. 62304153).

Data Availability Statement: The data are contained within the article and Supplementary Materials.

Acknowledgments: We would like to thank every teacher at the Centre for Advanced Materials and Printed Electronics Center, Tianjin University of Technology, for their excellent guidance.

Conflicts of Interest: The authors declare no conflicts of interest.

References

1. Teichner, S.J. The origins of photocatalysis. *J. Porous Mat.* **2008**, *15*, 311–314. [CrossRef]
2. Som, I.; Roy, M.; Saha, R. Advances in Nanomaterial-based Water Treatment Approaches for Photocatalytic Degradation of Water Pollutants. *ChemCatChem* **2020**, *12*, 3409–3433. [CrossRef]
3. Sanakousar, F.M.; Vidyasagar, C.C.; Jiménez-Pérez, V.M.; Prakash, K. Recent progress on visible-light-driven metal and non-metal doped ZnO nanostructures for photocatalytic degradation of organic pollutants. *Mater. Sci. Semicond. Process.* **2022**, *140*, 106390. [CrossRef]
4. MohammedSaleh Katubi, K.; Rasheed, A.; Ihsan, A.; Shaheen, B.; Alrowaili, Z.A.; Al-Buriahi, M.S.; Din, M.I.; Shakir, I.; Munir, S. Neodymium-doped nickel cobaltite reinforced with 2D MXene nanocomposite (Nd-$NiCo_2O_4$/MXene) for enhanced photocatalytic degradation of the organic pollutants. *Opt. Mater.* **2024**, *152*, 115390. [CrossRef]
5. Bhat, T.S.; Mali, S.S.; Sheikh, A.D.; Korade, S.D.; Pawar, K.K.; Hong, C.K.; Kim, J.H.; Patil, P.S. TiO_2/PbS/ZnS heterostructure for panchromatic quantum dot sensitized solar cells synthesized by wet chemical route. *Opt. Mater.* **2017**, *73*, 781–792. [CrossRef]
6. Bullock, R.M.; Das, A.K.; Appel, A.M. Surface Immobilization of Molecular Electrocatalysts for Energy Conversion. *Chem. A Eur. J.* **2017**, *23*, 7626–7641. [CrossRef]
7. Han, C.; Zhu, X.; Martin, J.S.; Lin, Y.; Spears, S.; Yan, Y. Recent Progress in Engineering Metal Halide Perovskites for Efficient Visible-Light-Driven Photocatalysis. *ChemSusChem* **2020**, *13*, 4005–4025. [CrossRef]
8. Han, S.T.; Xi, H.L.; Shi, R.X.; Fu, X.Z.; Wang, X.X. Prospect and progress in the semiconductor photocatalysis. *Chin. J. Chem. Phys.* **2003**, *16*, 339–349.
9. Zeng, Y.; Xu, Y.; Zhong, D.; Mou, J.; Yao, H.; Zhong, N. Visible-light responsive photocatalytic fuel cell with double Z-scheme heterojunction PTh/Ag_3PO_4/BiOI/Ti photoanode for efficient rhodamine B degradation and stable electricity generation. *Opt. Mater.* **2022**, *134*, 113103. [CrossRef]
10. Li, J.; Li, R.; Zou, L.; Liu, X. Efficient Degradation of Norfloxacin and Simultaneous Electricity Generation in a Persulfate-Photocatalytic Fuel Cell System. *Catalysts* **2019**, *9*, 835. [CrossRef]
11. Tan, X.; Bai, J.; Zheng, J.; Zhang, Y.; Li, J.; Zhou, T.; Xia, L.; Xu, Q.; Zhou, B. Photocatalytic fuel cell based on sulfate radicals converted from sulfates in situ for wastewater treatment and chemical energy utilization. *Catal. Today* **2019**, *335*, 485–491. [CrossRef]
12. Mohammadi, S.; Abdizadeh, H.; Golobostanfard, M.R. Effect of niobium doping on opto-electronic properties of sol–gel based nanostructured indium tin oxide thin films. *Ceram. Int.* **2013**, *39*, 4391–4398. [CrossRef]
13. Shi, Q.; Zhou, K.; Dai, M.; Hou, H.; Lin, S.; Wei, C.; Hu, F. Room temperature preparation of high performance AZO films by MF sputtering. *Ceram. Int.* **2013**, *39*, 1135–1141. [CrossRef]
14. Yates, H.M.; Evans, P.; Sheel, D.W.; Nicolay, S.; Ding, L.; Ballif, C. The development of high performance SnO_2:F as TCOs for thin film silicon solar cells. *Surf. Coat. Technol.* **2012**, *213*, 167–174. [CrossRef]
15. Shen, L.; Wang, Z.; Gong, Q.; Zhang, Y.; Wang, J. Photocatalytic Synthesis of Ultrafine Pt Electrocatalysts with High Stability Using TiO_2-Decorated N-Doped Carbon as Composite Support. *ChemSusChem* **2023**, *16*, e202300393. [CrossRef]
16. Fujishima, A.; Zhang, X.T. Titanium dioxide photocatalysis: Present situation and future approaches. *Comptes Rendus Chim.* **2006**, *9*, 750–760. [CrossRef]
17. Wang, X.; Zhao, Y.; Mølhave, K.; Sun, H. Engineering the Surface/Interface Structures of Titanium Dioxide Micro and Nano Architectures towards Environmental and Electrochemical Applications. *Nanomaterials* **2017**, *7*, 382. [CrossRef]
18. Kwon, C.H.; Shin, H.M.; Kim, J.H.; Choi, W.S.; Yoon, K.H. Degradation of methylene blue via photocatalysis of titanium dioxide. *Mater. Chem. Phys.* **2004**, *86*, 78–82. [CrossRef]

19. Lu, Y.; Deng, H.; Pan, T.; Wang, L.; Zhang, C.; He, H. Interaction between noble metals (Pt, Pd, Rh, Ir, Ag) and defect-enriched TiO_2 and its application in toluene and propene catalytic oxidation. *Appl. Surf. Sci.* **2022**, *606*, 154834. [CrossRef]
20. Andrianainarivelo, M.; Corriu, R.J.P.; Leclercq, D.; Mutin, P.H.; Vioux, A. Nonhydrolytic Sol−Gel Process: Aluminum Titanate Gels. *Chem. Mater.* **1997**, *9*, 1098–1102. [CrossRef]
21. Orel, B.; Lavrenčič-Štangar, U.; Hutchins, M.G.; Kalcher, K. Mixed phosphotungstic acid/titanium oxide gels and thin solid xerogel films with electrochromic-ionic conductive properties. *J. Non-Cryst. Solids* **1994**, *175*, 251–262. [CrossRef]
22. Li, R.; Ma, X.; Li, J.; Cao, J.; Gao, H.; Li, T.; Zhang, X.; Wang, L.; Zhang, Q.; Wang, G.; et al. Flexible and high-performance electrochromic devices enabled by self-assembled 2D TiO_2/MXene heterostructures. *Nat. Commun.* **2021**, *12*, 1587. [CrossRef] [PubMed]
23. Wang, J.-Y.; Huang, C.-S.; Ou, S.-L.; Cho, Y.-S.; Huang, J.-J. One-step preparation of TiO_2 anti-reflection coating and cover layer by liquid phase deposition for monocrystalline Si PERC solar cell. *Sol. Energy Mater. Sol. Cells* **2022**, *234*, 111433. [CrossRef]
24. Izutsu, H.; Nair, P.K.; Maeda, K.; Kiyozumi, Y.; Mizukami, F. Structure and properties of TiO_2 SiO_2 prepared by sol-gel method in the presence of tartaric acid. *Mater. Res. Bull.* **1997**, *32*, 1303–1311. [CrossRef]
25. Huang, J.Y.; Wang, Y.; Tao Fei, G.; Xu, S.H.; Zeng, Z.; Wang, B. TiO_2/ZnO double-layer broadband antireflective and down-shifting coatings for solar applications. *Ceram. Int.* **2023**, *49*, 11091–11100. [CrossRef]
26. Ge, S.; Sang, D.; Zou, L.; Yao, Y.; Zhou, C.; Fu, H.; Xi, H.; Fan, J.; Meng, L.; Wang, C. A Review on the Progress of Optoelectronic Devices Based on TiO_2 Thin Films and Nanomaterials. *Nanomaterials* **2023**, *13*, 1141. [CrossRef]
27. Zheng, Y.; Zhang, Y.; Wang, Y.; Yuan, F.; Gao, D.; Guo, Q.; Wang, L.; Hu, X. Enhanced photocatalytic degradation of xanthate over carbon quantum dots embedded on BiOI nanosheets under visible light. *Opt. Mater.* **2024**, *148*, 114890. [CrossRef]
28. Hu, X.; Han, W.; Zhang, M.; Li, D.; Sun, H. Enhanced adsorption and visible-light photocatalysis on TiO_2 with in situ formed carbon quantum dots. *Environ. Sci. Pollut. Res.* **2022**, *29*, 56379–56392. [CrossRef]
29. Li, J.; Liu, K.; Xue, J.; Xue, G.; Sheng, X.; Wang, H.; Huo, P.; Yan, Y. CQDS preluded carbon-incorporated 3D burger-like hybrid ZnO enhanced visible-light-driven photocatalytic activity and mechanism implication. *J. Catal.* **2019**, *369*, 450–461. [CrossRef]
30. Wang, X.; Zhao, W.; Lin, H.; Yao, C.; He, Y.; Ran, X.; Guo, L.; Li, T. Facet-dependent photocatalytic and photoelectric properties of CQDs/TiO_2 composites under visible irradiation. *J. Alloys Compd.* **2022**, *920*, 165896. [CrossRef]
31. Jung, D.; Kim, G.; Kim, M.-S.; Kim, B.-W. Evaluation of photocatalytic activity of carbon-doped TiO_2 films under solar irradiation. *Korean J. Chem. Eng.* **2012**, *29*, 703–706. [CrossRef]
32. Sendao, R.; de Yuso, M.D.M.; Algarra, M.; Silva, J.; da Silva, L.P. Comparative life cycle assessment of bottom-up synthesis routes for carbon dots derived from citric acid and urea. *J. Clean Prod.* **2020**, *254*, 10. [CrossRef]
33. Yang, Y.; Qiu, M.; Liu, L. TiO_2 nanorod array@carbon cloth photocatalyst for CO_2 reduction. *Ceram. Int.* **2016**, *42*, 15081–15086. [CrossRef]
34. Wang, C.Y.; Liu, Y.X.; Chen, R.; Zhu, X.; Ye, D.D.; Yang, Y.; Liao, Q. Gas diffusion TiO_2 photoanode for photocatalytic fuel cell towards simultaneous VOCs degradation and electricity generation. *J. Hazard. Mater.* **2023**, *447*, 130769. [CrossRef] [PubMed]
35. Sambandam, S.; Valluri, V.; Chanmanee, W.; de Tacconi, N.R.; Wampler, W.A.; Lin, W.Y.; Carlson, T.F.; Ramani, V.; Rajeshwar, K. Platinum-carbon black-titanium dioxide nanocomposite electrocatalysts for fuel cell applications. *J. Chem. Sci.* **2009**, *121*, 655–664. [CrossRef]
36. Wan, H.L.; Xu, B.Q.; Dai, Y.N.; Yang, B.; Liu, D.C.; Sen, W. Preparation of titanium powders by calciothermic reduction of titanium dioxide. *J. Cent. South Univ.* **2012**, *19*, 2434–2439. [CrossRef]
37. Xu, L.; Yang, L.; Bai, X.; Du, X.; Wang, Y.; Jin, P. Persulfate activation towards organic decomposition and Cr(VI) reduction achieved by a novel CQDs-TiO_2−x/rGO nanocomposite. *Chem. Eng. J.* **2019**, *373*, 238–250. [CrossRef]
38. Qian, X.; Yue, D.; Tian, Z.; Reng, M.; Zhu, Y.; Kan, M.; Zhang, T.; Zhao, Y. Carbon quantum dots decorated Bi_2WO_6 nanocomposite with enhanced photocatalytic oxidation activity for VOCs. *Appl. Catal. B Environ.* **2016**, *193*, 16–21. [CrossRef]
39. Zhou, T.; Chen, S.; Li, L.; Wang, J.; Zhang, Y.; Li, J.; Bai, J.; Xia, L.; Xu, Q.; Rahim, M.; et al. Carbon quantum dots modified anatase/rutile TiO_2 photoanode with dramatically enhanced photoelectrochemical performance. *Appl. Catal. B Environ.* **2020**, *269*, 118776. [CrossRef]
40. Patrocínio, A.O.T.; Paniago, E.B.; Paniago, R.M.; Iha, N.Y.M. XPS characterization of sensitized n-TiO_2 thin films for dye-sensitized solar cell applications. *Appl. Surf. Sci.* **2008**, *254*, 1874–1879. [CrossRef]
41. Liu, L.; Liu, Z.; Liu, A.; Gu, X.; Ge, C.; Gao, F.; Dong, L. Engineering the TiO_2–Graphene Interface to Enhance Photocatalytic H2 Production. *ChemSusChem* **2014**, *7*, 618–626. [CrossRef] [PubMed]
42. Li, J.H.; Zang, H.M.; Yao, S.; Li, Z.C.; Song, H. Photodegradation of benzothiazole ionic liquids catalyzed by titanium dioxide and silver-loaded titanium dioxide. *Chin. J. Chem. Eng.* **2020**, *28*, 1397–1404. [CrossRef]
43. Li, Y.; Lv, K.; Ho, W.; Dong, F.; Wu, X.; Xia, Y. Hybridization of rutile TiO_2 ($rTiO_2$) with g-C3N4 quantum dots (CN QDs): An efficient visible-light-driven Z-scheme hybridized photocatalyst. *Appl. Catal. B Environ.* **2017**, *202*, 611–619. [CrossRef]
44. Liu, R.; Li, H.; Duan, L.; Shen, H.; Zhang, Y.; Zhao, X. In situ synthesis and enhanced visible light photocatalytic activity of C-TiO_2 microspheres/carbon quantum dots. *Ceram. Int.* **2017**, *43*, 8648–8654. [CrossRef]
45. Martins, N.C.T.; Ângelo, J.; Girão, A.V.; Trindade, T.; Andrade, L.; Mendes, A. N-doped carbon quantum dots/TiO_2 composite with improved photocatalytic activity. *Appl. Catal. B Environ.* **2016**, *193*, 67–74. [CrossRef]

46. Rando, G.; Sfameni, S.; Milone, M.; Mezzi, A.; Brucale, M.; Notti, A.; Plutino, M.R.L. Smart pillar[5]arene-based PDMAEMA/PES beads for selective dye pollutants removal: Design, synthesis, chemical-physical characterization, and adsorption kinetic studies. *ChemSusChem* **2023**, *17*, e202301502. [CrossRef]
47. Jang, H.D.; Kim, S.-K.; Kim, S.-J. Effect of Particle Size and Phase Composition of Titanium Dioxide Nanoparticles on the Photocatalytic Properties. *J. Nanoparticle Res.* **2001**, *3*, 141–147. [CrossRef]
48. Shen, S.; Chen, J.; Wang, M.; Sheng, X.; Chen, X.; Feng, X.; Mao, S.S. Titanium dioxide nanostructures for photoelectrochemical applications. *Prog. Mater. Sci.* **2018**, *98*, 299–385. [CrossRef]
49. Luttrell, T.; Halpegamage, S.; Tao, J.; Kramer, A.; Sutter, E.; Batzill, M. Why is anatase a better photocatalyst than rutile?—Model studies on epitaxial TiO_2 films. *Sci. Rep.* **2014**, *4*, 4043. [CrossRef]
50. Gao, W.; Zhang, S.; Wang, G.; Cui, J.; Lu, Y.; Rong, X.; Gao, C. A review on mechanism, applications and influencing factors of carbon quantum dots based photocatalysis. *Ceram. Int.* **2022**, *48*, 35986–35999. [CrossRef]
51. Wang, J.; Tang, L.; Zeng, G.; Deng, Y.; Dong, H.; Liu, Y.; Wang, L.; Peng, B.; Zhang, C.; Chen, F. 0D/2D interface engineering of carbon quantum dots modified Bi_2WO_6 ultrathin nanosheets with enhanced photoactivity for full spectrum light utilization and mechanism insight. *Appl. Catal. B Environ.* **2018**, *222*, 115–123. [CrossRef]
52. Zhang, Z.L.; Wan, M.; Mao, Y.L. Enhanced photovoltaic effect of TiO_2-based composite $ZnFe_2O_4/TiO_2$. *J. Photochem. Photobiol. A Chem.* **2012**, *233*, 15–19. [CrossRef]
53. Pan, H.; Liao, W.; Sun, N.; Murugananthan, M.; Zhang, Y. Highly Efficient and Visible Light Responsive Heterojunction Composites as Dual Photoelectrodes for Photocatalytic Fuel Cell. *Catalysts* **2018**, *8*, 30. [CrossRef]
54. Zare, Z.; Tavakoli, O.; Parnian, M.J. Dual visible light photocatalytic fuel cell for efficient degradation of model organic pollutants using CdS/TiO_2 photoanode and TiO_2/CuS photocathode. *Chem. Pap.* **2024**, *78*, 3939–3957. [CrossRef]
55. Han, Z.; Zhong, D.; Xu, Y.; Chang, H.; Dong, L.; Liu, Y. Ag nanofilm enhanced S-type Ag@AgCl/tubular g-C_3N_4/Ti photoanode visible light response photocatalytic fuel cell. *Colloids Surf. A Physicochem. Eng. Asp.* **2024**, *691*, 133858. [CrossRef]